ΔE_{min} represents the ΔE minimum, V_{FM} is the FM nanoparticle volume and M_S is the saturation magnetization. $\mu_0 H_C = 1.3\,T$ is calculated for the parameter values of AFM sublattice magnetization[5] $\mu_0 M' = 1.8\,T$, a molecular field[5] coefficient between the AFM sublattices of $w = 100$, an AFM second-order anisotropy constant of $K_1 = 2.7 \times 10^7\,J\,m^{-3}$ (ref. 27), $V_{FM} = 33.5\,nm^3$ and $\mu_o H_{ex} = 84\,T$ (ref. 28). Considering the uncertainty in the values of most of these parameters, the agreement with the experimental value, $\mu_0 H_C = 0.76\,T$, is very satisfactory. Unlike the usual exchange-bias systems, the calculated and experimental values of the coercive field are in agreement. Owing to their very small size, the FM particles can be thought of as being coupled to a unique AF domain, and consequently there is no competition between different coupling terms.

Additionally, exchange coupling at the Co/CoO interface gives rise to a shift of the hysteresis loop along the field axis. The large bias fields observed may be shown to suggest the existence of AFM non-collinear moment configurations, reminiscent of spin-glass configurations. Such configurations exist in magnetic oxide nanoparticles[29,30], and, by analogy, they may be expected at the surface of small cavities.

In all the above discussion, a compensated Co/CoO interface has been assumed. Coupling energies of the same order of magnitude could be obtained in the case of large uncompensation, of the order of 30%, existing at the Co/CoO interface. However, in this case a significant part of the FM signal would originate from the uncompensated moments in the matrix. The measurements on the Ag/CoO sample do not reveal such signal, and large uncompensation can thus be realistically excluded.

The present results demonstrate that the magnetic coupling of FM nanoparticles with an AFM matrix is a source of a large effective additional anisotropy. This leads to a marked improvement in the thermal stability of the moments of the FM nanoparticles—we observed an increase in the blocking temperature, T_B, of almost two orders of magnitude. This mechanism provides a way to beat the 'superparamagnetic limit' in isolated particles. Although it is clear that the system examined here is not suitable in itself for application, the approach developed should in principle apply to nanoparticles deposited on a single AFM layer, a structure suitable for use as a recording medium. With the right choice of FM and AFM components, exchange anisotropy coupling could ultimately allow magnetically stable dots only a few nanometres in size: such dots would surpass the storage-density goal of 1 Tbit in^{-2}, as set by the magnetic-storage industry. □

Received 24 December 2002; accepted 22 April 2003; doi:10.1038/nature01687.

1. Kodama, R. H. Magnetic nanoparticles. *J. Magn. Magn. Mater.* **200,** 359–372 (1999).
2. Martín, J. I. *et al.* Ordered magnetic nanostructures: Fabrication and properties. *J. Magn. Magn. Mater.* **256,** 449–501 (2003).
3. Sun, S. H. *et al.* Monodisperse FePt nanoparticles and ferromagnetic FePt nanocrystal superlattices. *Science* **287,** 1989–1992 (2000).
4. Häfeli, U., Schütt, W., Teller, J. & Zborowski, M. (eds) *Scientific and Clinical Applications of Magnetic Materials* (Plenum, New York, 1997).
5. Chikazumi, S. *Physics of Ferromagnetism* (Oxford Univ. Press, New York, 1997).
6. Weller, D. & Moser, A. Thermal effect limits in ultrahigh-density magnetic recording. *IEEE Trans. Magn.* **35,** 4423–4439 (1999).
7. Thompson, D. A. & Best, J. S. The future of data storage technology. *IBM J. Res. Dev.* **44,** 311–322 (2000).
8. Meiklejohn, W. H. & Bean, C. P. New magnetic anisotropy. *Phys. Rev.* **102,** 1413–1414 (1956).
9. Nogués, J. & Schuller, I. K. Exchange bias. *J. Magn. Magn. Mater.* **192,** 203–232 (1999).
10. Huberland, H. *et al.* Thin film growth from energetic cluster impact: A feasibility study. *J. Vac. Sci. Technol. A* **10,** 3266–3271 (1992).
11. Gangopadhyay, S. *et al.* Exchange anisotropy in oxide passivated Co fine particles. *J. Appl. Phys.* **73,** 6964–6966 (1993).
12. Luis, F. *et al.* Magnetic relaxation of interacting Co clusters: Crossover from two- to three-dimensional lattices. *Phys. Rev. Lett.* **88,** 217205 (2002).
13. García-Otero, J. *et al.* Influence of dipolar interaction on magnetic properties of ultrafine ferromagnetic particles. *Phys. Rev. Lett.* **84,** 167–170 (2000).
14. Gu, E. *et al.* Two-dimensional paramagnetic-ferromagnetic phase transition and magnetic anisotropy in Co(110) epitaxial nanoparticle arrays. *Phys. Rev. B* **60,** 4092–4095 (1999).
15. Parent, F. *et al.* Giant magnetoresistance in Co-Ag granular films prepared by low-energy cluster beam deposition. *Phys. Rev. B* **55,** 3683–3687 (1997).
16. Held, G. A. *et al.* Competing interactions in dispersions of superparamagnetic nanoparticles. *Phys. Rev. B* **64,** 012408 (2001).
17. Woods, S. I. *et al.* Direct investigation of superparamagnetism in Co nanoparticle films. *Phys. Rev. Lett.* **87,** 137205 (2001).
18. Murray, C. B. *et al.* Monodisperse 3d transition-metal (Co,Ni,Fe) nanoparticles and their assembly into nanoparticle superlattices. *Mater. Res. Soc. Bull.* **26,** 985–991 (2001).
19. Sako, S., Osshima, K. & Saki, M. Magnetic property of oxide passivated Co nanosized particles dispersed in two dimensional plane. *J. Phys. Soc. Jpn* **70,** 2134–2138 (2001).
20. Lund, M. S. *et al.* Effect of anisotropy on the critical antiferromagnetic thickness in exchange biased bilayers. *Phys. Rev. B* **66,** 054422 (2002).
21. Peng, D. L. *et al.* Magnetic properties of monodispersed Co/CoO clusters. *Phys. Rev. B* **61,** 3103–3109 (2000).
22. Sort, J. *et al.* Room temperature coercivity enhancement in mechanically alloyed antiferromagnetic-ferromagnetic powders. *Appl. Phys. Lett.* **75,** 3177–3179 (1999).
23. Liu, K. *et al.* Fabrication and thermal stability of arrays of Fe nanodots. *Appl. Phys. Lett.* **81,** 4434–4436 (2002).
24. Jensen, P. J. Magnetic recording medium with improved temporal stability. *Appl. Phys. Lett.* **78,** 2190–2192 (2001).
25. Schulthess, T. C. & Butler, W. H. Consequences of spin-flop coupling in exchange biased films. *Phys. Rev. Lett.* **81,** 4516–4519 (1998).
26. Stamps, R. L. Mechanisms for exchange bias. *J. Phys. D* **33,** R247–R268 (2000).
27. Kanamori, J. Theory of the magnetic properties of ferrous and cobaltous oxides. *Prog. Theor. Phys.* **17,** 177–196 (1957).
28. Takano, K. *et al.* Interfacial uncompensated antiferromagnetic spins: Role of unidirectional anisotropy in polycrystalline $Ni_{81}Fe_{19}$/CoO bilayers. *Phys. Rev. Lett.* **79,** 1130–1133 (1997).
29. Kodama, R. H., Makhlouf, S. H. & Berkowitz, A. E. Finite size effects in antiferromagnetic NiO nanoparticles. *Phys. Rev. Lett.* **79,** 1393–1396 (1997).
30. Coey, J. M. D. Noncollinear spin arrangement in ultrafine ferrimagnetic crystallites. *Phys. Rev. Lett.* **27,** 1140–1143 (1971).

Acknowledgements We thank N. Dempsey for critical reading of the manuscript, and D. Weller for discussions. This work was partly supported by the US National Science Foundation, Seagate Technology, the Catalan Direcció General de Recerca, and the Spanish Comisión Interministerial de Ciencia y Tecnología.

Competing interests statement The authors declare that they have no competing financial interests.

Correspondence and requests for materials should be addressed to V.S. (vassil@udel.edu).

Sea-level fluctuations during the last glacial cycle

M. Siddall*, E. J. Rohling*, A. Almogi-Labin†, Ch. Hemleben‡, D. Meischner§, I. Schmelzer‡ & D. A. Smeed*

* *Southampton Oceanography Centre, European Way, Southampton SO14 3ZH, UK*
† *Geological Survey of Israel, 30 Malkhe Yisrael Street, Jerusalem 95501, Israel*
‡ *Department of Geology and Paleontology, University of Tuebingen, Sigwartstrasse 10, D-7400, Tuebingen, Germany*
§ *Department of Sedimentary Geology, Institute for Geology and Paleontology, University of Göttingen, 37073 Göttingen, Germany*

The last glacial cycle was characterized by substantial millennial-scale climate fluctuations[1–5], but the extent of any associated changes in global sea level (or, equivalently, ice volume) remains elusive. Highstands of sea level can be reconstructed from dated fossil coral reef terraces[6,7], and these data are complemented by a compilation of global sea-level estimates based on deep-sea oxygen isotope ratios at millennial-scale resolution[8] or higher[1]. Records based on oxygen isotopes, however, contain uncertainties in the range of ±30 m, or ±1 °C in deep sea temperature[9,10]. Here we analyse oxygen isotope records from Red Sea sediment cores to reconstruct the history of water residence times in the Red Sea. We then use a hydraulic model of the water exchange between the Red Sea and the world ocean to derive the sill depth—and hence global sea level—over the past 470,000 years (470 kyr). Our reconstruction is accurate to within ±12 m, and gives a centennial-scale resolution from 70 to 25 kyr before present. We

find that sea-level changes of up to 35 m, at rates of up to 2 cm yr^{-1}, occurred, coincident with abrupt changes in climate.

This study takes advantage of the fact that the Red Sea is extremely sensitive to sea-level change, as a consequence of the narrow (18 km) and shallow (137 m) character of its only connection with the open ocean (the Strait of Bab el Mandab). Reduction of the strait profile by sea-level lowering decreases the exchange transport of water masses through the strait. This results in increased residence times of the water within the Red Sea, enhancing the effect of the high rate of evaporation (2.06 m yr^{-1})[11] on properties in the Red Sea. The basin thus amplifies the signals of sea-level change, which are recorded in $\delta^{18}O$ values of foraminifera in Red Sea sediment cores. This amplification has been previously used to calculate sea-level lowstands at times of maximum glaciation during the past 500 kyr (ref. 12), which have since been independently corroborated[9].

To unlock the potential of Red Sea data for the development of continuous sea-level records (rather than only lowstands) in a manner that is independent of existing methods, we combine a realistic representation of exchange flow in the Strait of Bab el Mandab[13] with an eddy flux parameterization to represent the Red Sea basin[14]. We then calculate salinity and, using routines described previously for the Mediterranean Sea[15], $\delta^{18}O$ for calcite in equilibrium with ambient water. Changes in the modelled salinity and $\delta^{18}O$ values are dominated by sea level, and the simulated behaviour of $\delta^{18}O$ with sea-level change is then applied to translate $\delta^{18}O$ records from sediment cores into records of past sea-level change. For this purpose, records are selected from relatively shallow (<1,000 m) locations away from the axial trough of the Red Sea, to avoid potential hot-brine-related diagenetic alterations of the foraminiferal calcite.

To ensure that our reconstructions account for any potential change in the basin's climatic forcing through time, we determine a 2σ equivalent confidence limit to our sea-level reconstructions by means of sensitivity tests. These comprise extreme scenarios for the annually integrated evaporation and relative humidity, and an additional temperature uncertainty (see Supplementary Information). Before applying the method to the millennial-scale variability of the last glacial cycle, we discuss several validation exercises that compare our sea-level results with those from other methods.

We resolve exchange transport through the strait in of terms hydraulic control[13,16]. Observations[17] and hydraulic modelling[13] for the present day suggest that exchange of waters across the sill at Hanish is sub-maximal. This is due to the dominant effect of the summer (southwestern) monsoon on the modern Red Sea. It causes upwelling of Gulf of Aden Intermediate Water (GAIW) in the Gulf of Aden, which in turn intrudes into the Red Sea as an intermediate layer[17]. The hydraulic model realistically represents this intrusion of GAIW between July and September[13,16]. At lower sea levels, Hanish sill would be shallower and the GAIW upwelling would have to intensify for the intrusion to occur. Consequently, the sensitivity of the Red Sea to monsoonal variability is reduced at lower sea levels. In a simulation with sea level approximately 120 m lower than today, we find maximal exchange at Hanish sill, with flow over the sill reaching an upper limit determined by the sill geometry and evaporation over the Red Sea. That result corroborates the assumption of maximal exchange at glacial times made in previous studies[12].

The combined 'hydraulic + basin' model conserves buoyancy in the Red Sea so that $Q_3 g' = BLW$, where Q_3 is the volume flux leaving the Red Sea in the lower layer, g' is the reduced gravity, B is the buoyancy flux through the surface of the Red Sea (3.4×10^{-8} m^2 s^{-3}), L is the length of the basin (1,960 km) and W is the width of the basin, which varies with sea level. The buoyancy transport within the basin is limited by a maximum eddy flux[14] $Q_3 = kh_1^2 Wg'/fL$, where f is the Coriolis parameter, Q_1 is the flux in the Red Sea in the upper layer, h_1 is the thickness of the upper layer in the Red Sea and k is a constant. Technical details of the model, including an evaluation of the procedures applied, are presented in Supplementary Information.

Although the strait exchange is seasonally resolved, the model basin responds only to the annually integrated sill exchange. Previous hydraulic modelling of the exchange indicates that this is a reasonable approximation[13], and it allows important basin forcing parameters—evaporation and humidity—to be kept constant throughout the annual cycle. The main run uses evaporation and relative humidity at their modern annually averaged levels of

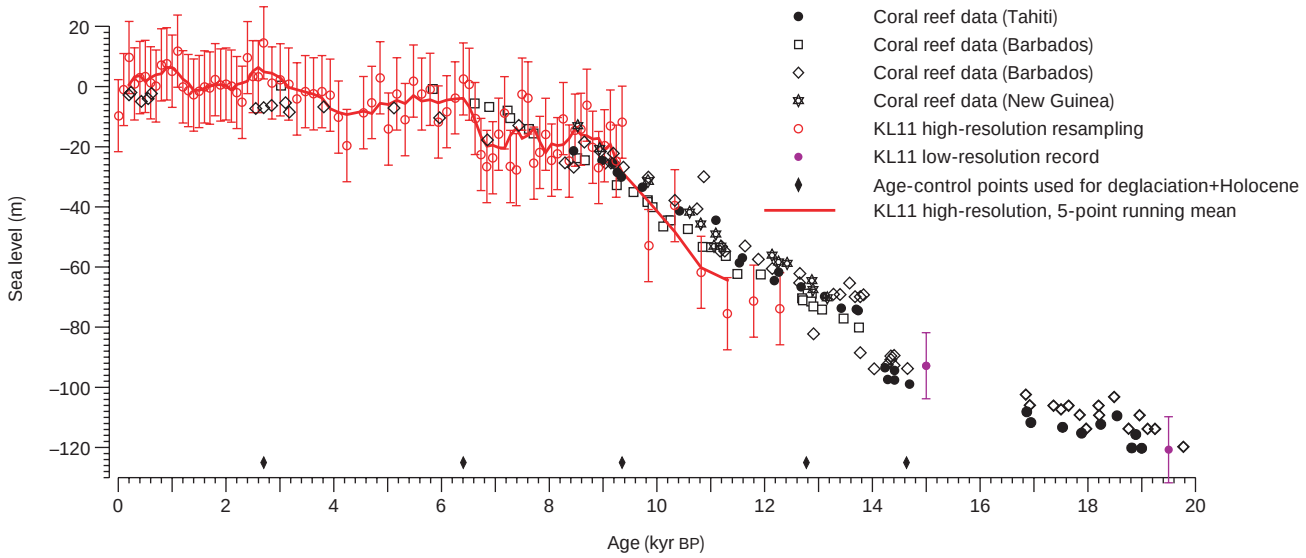

Figure 1 Sea-level reconstruction since the start of the Younger Dryas, based on the $\delta^{18}O$ record from core KL11 (18° 44.5′ N, 39° 20.6′ E) including error bars of ±12 m. Chronology is based on calibrated AMS radiocarbon datings[20]. The record is zeroed to modern sea level by removing the mean KL11 record for the past 7 kyr. The point from the low-resolution record of KL11 reported in the LGM is based on intercalibrated benthic $\delta^{18}O$ data[19]. Black symbols are sea-level values obtained from coral reef studies[21–24].

2.06 m yr^{-1} (ref. 11) and 70% (ref. 18), respectively. Sea surface temperature is set to decrease linearly with respect to sea level, so that it reaches a value 5 °C lower than today at the Last Glacial Maximum (LGM) (Supplementary Information). Sensitivity tests allow for a ±2 °C uncertainty in temperature in addition to changes in evaporation between 2.8 m yr^{-1} and 1.4 m yr^{-1} and in relative humidity between 60% and 80%, the modern seasonal extremes[11,18]. Increases in global ice volume concentrate salinity by ~0.01 p.s.u. and $\delta^{18}O$ by ~0.01‰ per metre of sea-level fall[15,10]. Monsoonal upwelling of GAIW is kept similar to the present throughout the experiments, so that the upper interface of GAIW shallows and deepens to the same extent through the seasonal cycle (that is, sinusoidally from 20 m below the surface in mid-July to 110 m below the surface in mid-January[13]).

Strictly speaking, our sea-level reconstructions pertain to the level at Bab el Mandab, which may deviate somewhat from truly global changes owing to uplift and isostatic effects. Uplift of the strait was previously estimated at 0.044 ± 0.022 m kyr^{-1} (ref. 12), and the 470-kyr reconstruction presented here optimizes the agreement with existing data for a rate of 0.02 m kyr^{-1}. Isostatic effects are probably negligible compared to the confidence limits of our method, in view of the landlocked and narrow character of the Red Sea/Gulf of Aden and the great distance from continental ice sheets. Our reconstructions therefore offer close approximations of global sea level (and hence, ice volume), especially during the last glacial cycle, the focus of this study.

We first apply our method to reconstruct sea-level changes since the onset of the Younger Dryas, based on a $\delta^{18}O$ series from recent high-resolution resampling of this interval in central Red Sea core GEOTUE-KL11 (referred to here as KL11)[19,20], for validation against the sea-level record from coral-reef data[21–24] (Fig. 1). There is no record from the Red Sea for the LGM and the deglaciation before the onset of the Younger Dryas, because of the presence of a so-called 'aplanktonic' interval. Such intervals characterize severe glacial maxima throughout the central and northern Red Sea, and have been related to salinities in excess of 49–50 p.s.u. (refs 12, 19, 25). The sea-level value given for the LGM in KL11 (Fig. 1) derives from intercalibrated $\delta^{18}O$ measurements of benthic foraminifera[19], and it agrees well with lowstand estimates from the coral reefs. The rest of the sea-level reconstruction from our method also compares favourably with the coral-reef record. Given that the sensitivity of our sea-level method to climatic uncertainties is ±12 m (equivalent to 2σ confidence limits), the observed deviations of up to 5 m from the mean for individual samples are exactly what should be expected from analyses of a random specimen collection from discrete core samples that integrate decadal, interannual and seasonal climatic variability. Changes in sea level greater than ±12 m are outside this uncertainty, and hence are considered real.

Next, we compare sea-level reconstructions based on two independent central Red Sea records that both cover several glacial–interglacial cycles, down to 471 kyr before present (BP): cores KL11[19,20] and MD921017[12,25] (Fig. 2a). Their close similarity shows the reproducibility of our method (Fig. 2d). This long-core exercise also validates our sea-level reconstructions relative to those from other techniques over the entire glacial–interglacial climate range (Fig. 2c). The good agreement is a clear indication that our ±12 m confidence limit adequately captures the full range of uncertainty about climatic forcing values. As an additional benefit, our model offers a quantitative expression of the Red Sea salinity history (Fig. 2b).

Having thus validated this method's capacity to reconstruct sea level with a realistic confidence limit, it is subsequently applied to evaluate any sea-level changes associated with millennial-scale climate fluctuations within the interval 70–25 kyr BP. It was previously established that the influences of the southwestern monsoon did not reach the Red Sea/Gulf of Aden region at those times[25,26], effectively 'locking' the basin in the present-day winter mode. A discussion of Red Sea insensitivity to monsoon variability is given in Supplementary Information. Hence, the ±12-m confidence margin to our reconstructions is rather generous as far as this period is concerned.

The 70–25 kyr BP interval in core KL11 was resampled at an average 200-yr resolution, and a $\delta^{18}O$ record was constructed for *Globigerinoides ruber*[20], similar to the previously mentioned long-core and deglaciation records of KL11 and MD921017. An initial rough chronology was established from isotope stratigraphy in the long-core record of KL11[19] (Fig. 2) and from accelerator mass spectrometry (AMS) ^{14}C datings, calibrated[27] using a 400-yr reservoir age[20] (Fig. 3a). A recent high-resolution deep-sea $\delta^{18}O$ study[1] suggests that millennial-scale sea-level variability during the last glacial cycle should resemble, in both timing and structure, the Antarctic temperature history recorded in ice-core $\delta^{18}O$ and δD data[2,3]. To refine the initial chronology for the 70–25 kyr BP interval in KL11, therefore, we focused on synchronization with the high-resolution Antarctic records (Fig. 3b). There is a remarkable signal similarity (Fig. 3d, e). To refine the initial chronology for the 70–25 kyr BP interval in KL11, therefore, we focused on synchronization with the high-resolution Antarctic records (Fig. 3b, c). There is a remarkable signal similarity (Fig. 3d, e).

Application of our sea-level method to the highly resolved 70–25 kyr BP $\delta^{18}O$ series of central Red Sea core KL11 yields a record of sea-level variability that agrees well with fossil-reef data[6,7] (Fig. 4a). We also compare our result with a scaled plot of the high-resolution deep-sea $\delta^{18}O$ record of eastern North Atlantic core MD952042[1],

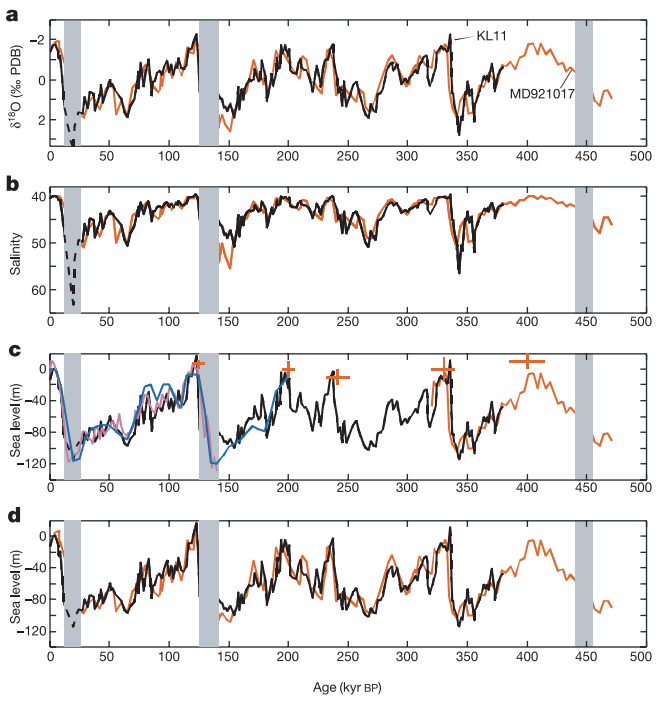

Figure 2 Sea-level reconstruction for the Red Sea for the past 470 kyr. **a**, The long-timescale oxygen isotope records of cores KL11[19](black line) and MD921017 (19° 23.24′ N, 38° 40.84′ E)[12,25] (red line). Grey bands indicate aplanktonic periods in the record. An LGM value based on intercalibrated $\delta^{18}O$ data[19] is indicated with a dashed line. **b**, The model-generated salinity record from core KL11 (black line) extended with core MD921017 (red line). Salinity in p.s.u. (practical salinity units). **c**, The modelled long-term sea-level record from core KL11 (black line) extended with the record from core MD921017[12,25] (red line). The pink and blue lines are given for comparison, and represent sea-level compilations from deep-sea oxygen isotope and coral-reef data[8,22]. Red crosses and bars represent a summary of estimates from several studies[7,9,12,28,29]. **d**, Comparison of the modelled sea levels from cores KL11 (black line) and MD921017 (red line).

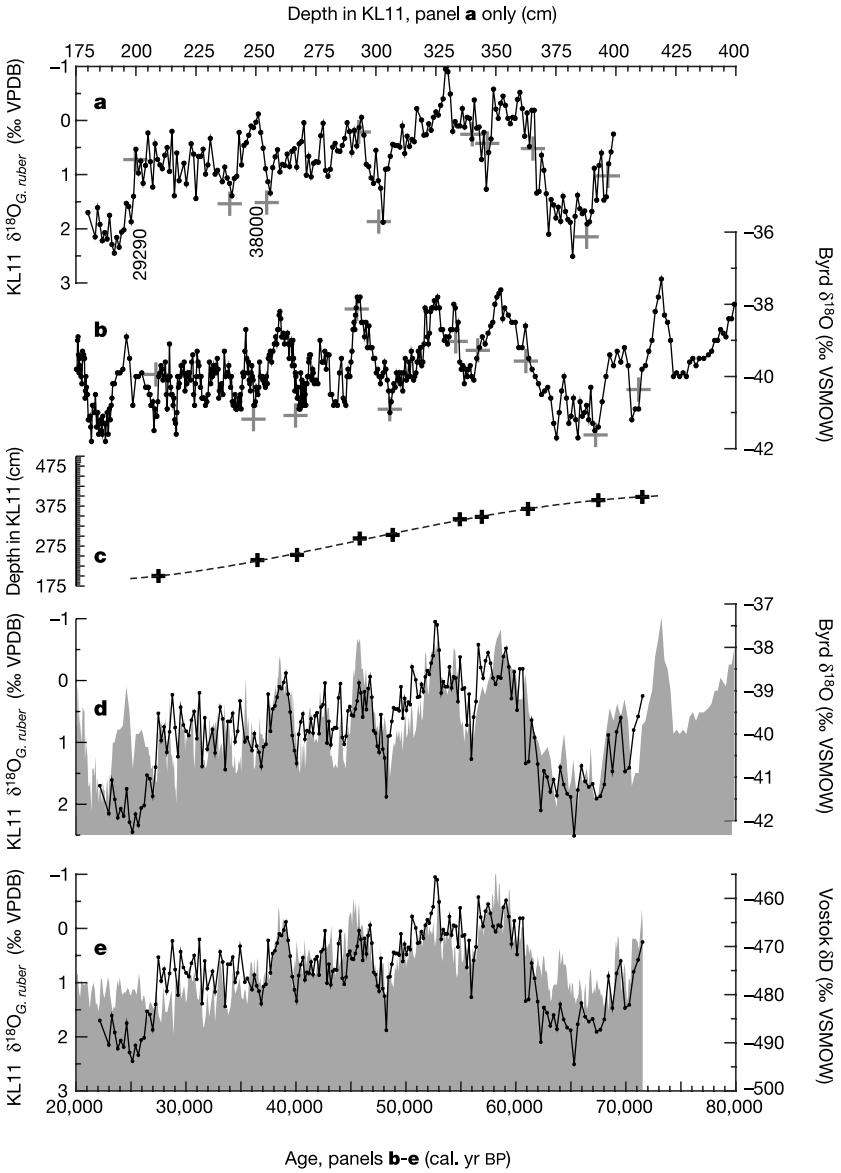

Figure 3 The high-resolution $\delta^{18}O$ record for the study interval between ~70 and ~20 kyr BP, based on analyses of the planktonic foraminifer *G. ruber* in central Red Sea core KL11[19,20]. **a**, Original data versus depth in the core. Grey crosses indicate tie-points used to relate the chronology of KL11 to the West Antarctic Byrd ice-core $\delta^{18}O$ series[3]. Numbers shown are (AMS) ^{14}C datings, calibrated using a 400-yr reservoir age. **b**, The Byrd $\delta^{18}O$ record versus Greenland GISP2 ice-core equivalent age, based on synchronization of abrupt changes in the methane concentrations within the two ice cores[3]. Grey crosses indicate tie points as described for **a**. The youngest tie-point is selected in a position nearest to the age suggested by the AMS ^{14}C dating in KL11. This also allows for the fact that the Byrd record is different from the East Antarctic Vostok δD series (**e**) in the interval ~25–17 kyr BP, possibly owing to a regional West Antarctic climate fluctuation[2]. **c**, Depths of tie points in KL11 versus their equivalent age in the Byrd record. Dashed line represents a smooth fit through the tie-points for conversion of KL11 depths into age. **d**, KL11 $\delta^{18}O$ series after conversion to age as in **c**, superimposed upon the Byrd $\delta^{18}O$ series to illustrate the remarkable similarity in the signal structures. **e**, As **d** but using the Vostok δD record.

which—although not yet translated into absolute sea-level values—shows a good signal agreement with our sea-level reconstruction. The agreement is especially notable when the age model of KL11 is 'tuned' to that of independently dated MD952042 (Fig. 4b). The only realistic influences on the deep-sea $\delta^{18}O$ record of MD952042 are global ice volume (hence, sea level) and deep-sea temperature changes. A ±1 °C uncertainty in deep-sea temperature variations implies a confidence limit of about ±30 m on inferred sea levels, based on a 0.26‰ change in the water-to-calcite isotopic fractionation per 1 °C, and a 0.008‰ change in Atlantic deep-sea $\delta^{18}O_{water}$ per metre sea-level lowering[10]. Offsets between the records (Fig. 4) that exceed ±12 m around our reconstruction may be due to analytical uncertainty, and/or deep-sea temperature changes affecting MD952042.

We have presented here an independent method for sea-level reconstruction that is applicable over timescales from glacial–interglacial to centennial. The reconstruction for the 70–25 kyr BP interval offered here is to our knowledge the first to be sufficiently resolved—in both the temporal sense and in terms of the confidence margin—to determine the realistic magnitudes and rates of sea-level shifts associated with millennial-scale climate fluctuations. We have corroborated an earlier report of signal similarity between the Antarctic temperature history and the sea-level record[1]. Also, we have derived a magnitude of the sea-level shifts during the 70–25 kyr

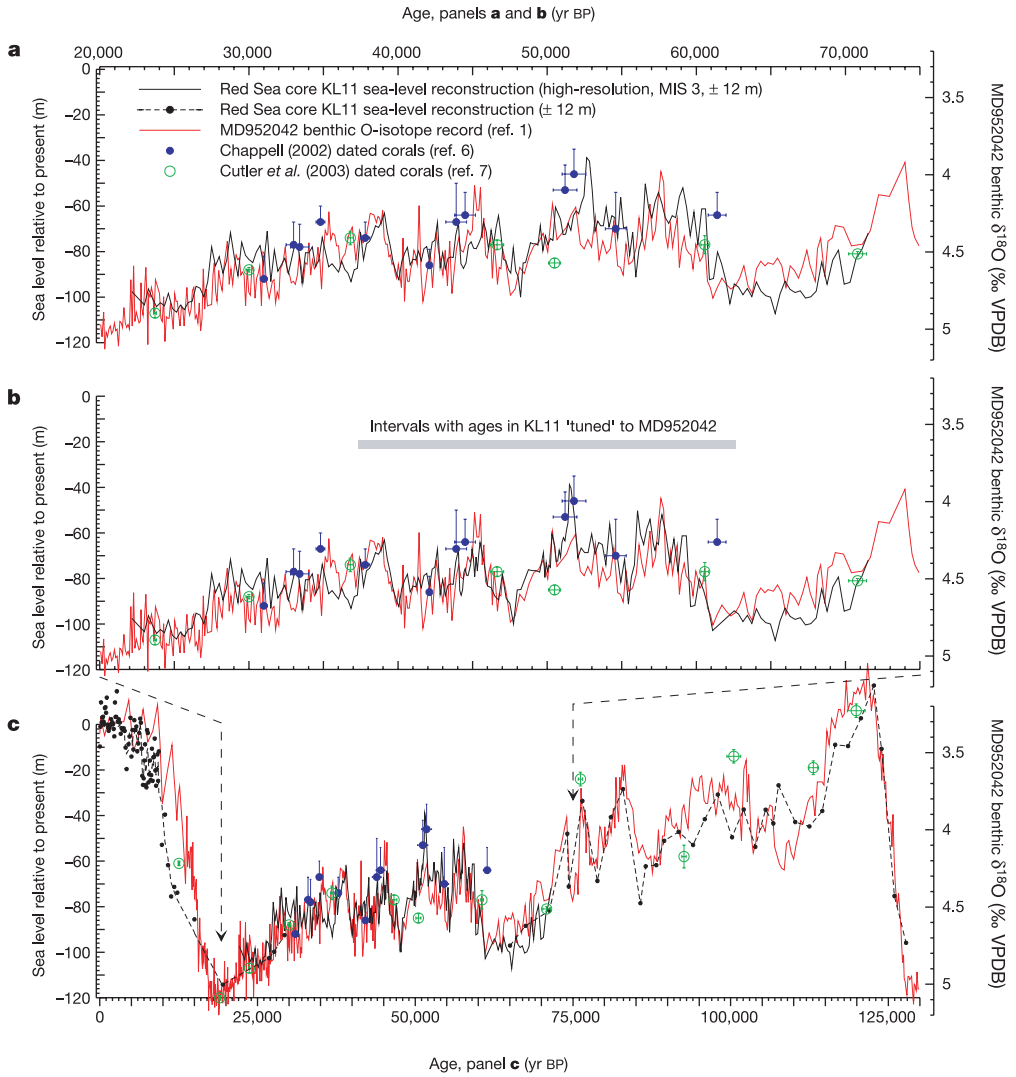

Figure 4 Comparison between the Red Sea and other sea-level estimates. **a**, The modelled high-resolution sea-level reconstruction for the period between 20 and 75 kyr BP from core KL11 (timescale as developed in Fig. 3). **b**, As **a** but with the KL11 timescale fine tuned to the independently derived timescale of MD952042 (where possible on the basis of signal similarity). **c**, Red Sea sea level reconstruction between 0 and 130 kyr BP combining both high and low resolution records of core KL11.

BP interval of up to 35 ± 12 m, more than twice the volume of the Greenland and West Antarctic ice sheets. The maximum rate of change of ~0.02 m yr^{-1} is similar to the mean rate of change during the last deglaciation. □

Received 28 January; accepted 24 April 2003; doi:10.1038/nature01690.

1. Shackleton, N. J., Hall, M. A. & Vincent, E. Phase relationships between millennial-scale events 64,000–24,000 years ago. *Paleoceanography* **15,** 565–569 (2000).
2. Blunier, T. *et al.* Asynchrony of Antarctic and Greenland climate change during the last glacial period. *Nature* **394,** 739–743 (1998).
3. Blunier, T. & Brook, E. Timing of millennial-scale climate change in Antarctica and Greenland during the last glacial period. *Science* **291,** 109–112 (2001).
4. Dansgaard, W. *et al.* Evidence for general instability of past climate from a 250-kyr ice-core record. *Nature* **364,** 218–220 (1993).
5. Grootes, P. M., Stuiver, M., White, J. W. C., Johnsen, S. J. & Jouzel, J. Comparison of oxygen isotope records from the GISP2 and GRIP Greenland ice cores. *Nature* **366,** 552–554 (1993).
6. Chappell, J. Sea-level changes forced ice breakouts in the last glacial cycle: New results from coral terraces. *Quat. Sci. Rev.* **21,** 1229–1240 (2002).
7. Cutler, K. B. *et al.* Rapid sea-level fall and deep-ocean temperature change since the last interglacial period. *Earth Planet. Sci. Lett.* **206,** 253–271 (2003).
8. Shackleton, N. J. Oxygen isotopes, ice volume and sea level. *Quat. Sci. Rev.* **6,** 183–190 (1987).
9. Waelbroeck, C. *et al.* Sea-level and deep water temperature changes derived from benthic foraminifera isotopic records. *Quat. Sci. Rev.* **21,** 295–305 (2002).
10. Adkins, J. F., McIntyre, K. & Schrag, D. P. The salinity, temperature, and delta O-18 of the glacial deep ocean. *Science* **298,** 1769–1773 (2002).
11. Sofianos, S. S., Johns, W. & Murray, S. P. Heat and freshwater budgets in the Red Sea from direct observations at Bab el Mandab. *Deep Sea Res. II* **49,** 1323–1340 (2002).
12. Rohling, E. J. *et al.* Magnitudes of sea-level lowstands of the past 500,000 years. *Nature* **394,** 162–165 (1998).
13. Siddall, M., Smeed, D. A., Matthiesen, S. & Rohling, E. J. Modelling the seasonal cycle of the exchange flow in Bab el Mandab (Red Sea). *Deep Sea Res. I* **49,** 1551–1569 (2002).
14. Griffiths, R. W. & Hopfinger, E. J. The structure of mesoscale turbulence and horizontal spreading at ocean fronts. *Deep Sea Res.* **31,** 245–269 (1984).
15. Rohling, E. J. Environmental control on Mediterranean salinity and $\delta^{18}O$. *Paleoceanography* **14,** 706–715 (1999).
16. Smeed, D. A. Hydraulic control of three-layer exchange flows: Application to the Bab-al-Mandab. *J. Phys. Oceanogr.* **30,** 2574–2588 (2000).
17. Smeed, D. A. Seasonal variation of the flow in the strait of Bab al Mandab. *Oceanol. Acta* **20,** 773–781 (1997).
18. Edwards, F. J. in *Key Environments: Red Sea* (eds Edwards, A. J. & Head, S. M.) 45–69 (Oxford, Pergamon, 1987).
19. Hemleben, C. *et al.* Three hundred and eighty thousand year-long stable isotope and faunal records from the Red Sea. *Paleoceanography* **11,** 147–156 (1996).
20. Schmelzer, I.. *High-frequency Event Stratigraphy and Paleoceanography of the Red Sea* Thesis, Eberhard-Karls-Univ. (1998).
21. Fairbanks, R. G. The age and origin of the "Younger Dryas climate event" in Greenland ice cores. *Paleoceanography* **5,** 937–948 (1990).
22. Bard, E., Hamelin, B., Fairbanks, R. G. & Zindler, A. Calibration of the ^{14}C timescale over the past 30,000 years using mass spectrometric U–Th ages from Barbados corals. *Nature* **345,** 405–409 (1990).
23. Edwards, R. L. *et al.* A large drop in atmospheric ^{14}C and reduced melting in the Younger Dryas documented by ^{230}Th ages of corals. *Science* **260,** 962–968 (1993).

24. Bard, E. *et al.* Deglacial sea-level record from Tahiti corals and the timing of global meltwater discharge. *Nature* **382,** 241–244 (1996).
25. Fenton, M., Geiselhart, S., Rohling, E. J. & Hemleben, C. Aplanktonic zones in the Red Sea. *Mar. Micropaleontol.* **40,** 277–294 (2000).
26. Almogi-Labin, A. *et al.* The influence of the NE winter monsoon on productivity changes in the Gulf of Aden, NW Arabian Sea, during the last 530 ka as recorded by foraminifera. *Mar. Micropaleontol.* **40,** 295–319 (2000).
27. Voelker, A. H. L. *et al.* Correlation of marine ^{14}C ages from the Nordic Seas with the GISP2 isotope record: Implications for radiocarbon calibration beyond 25 ky BP. *Radiocarbon* **40,** 517–553 (1998).
28. Pirazzoli, P. A. *et al.* A one million year sequence of marine terraces on Sumba Island, Indonesia. *Mar. Geol.* **109,** 221–236 (1993).
29. Gallup, C. D., Edwards, R. L. & Johnson, R. G. The timing of high sea levels over the past 200,000 years. *Science* **263,** 796–800 (1994).

Supplementary Information accompanies the paper on **www.nature.com/nature**.

Acknowledgements We thank N. Shackleton for advice and permission to use the deep-sea $\delta^{18}O$ record of MD952042b, E. Bard for Tahiti sea-level estimates, and A. Hogg, J. F. McManus, P. M. Grootes and H. Erlenkeuser for help during the preparation of this Letter. M.S. has been funded by a NERC studentship.

Competing interests statement The authors declare that they have no competing financial interests.

Correspondence and requests for materials should be addressed to M.S. (ms14@soc.soton.ac.uk).

Archaean ultra-depleted komatiites formed by hydrous melting of cratonic mantle

A. H. Wilson*, S. B. Shirey† & R. W. Carlson†

** School of Geological and Computer Sciences, University of Natal, Durban 4041, South Africa*
† Department of Terrestrial Magnetism, Carnegie Institution of Washington, 5241 Broad Branch Road, Washington DC 20015, USA

Komatiites are ultramafic volcanic rocks containing more than 18 per cent MgO (ref. 1) that erupted mainly in the Archaean era (more than 2.5 gigayears ago). Although such compositions occur in later periods of Earth history (for example, the Cretaceous komatiites of Gorgona Island[2]), the more recent examples tend to have lower MgO content than their Archaean equivalents. Komatiites are also characterized by their low incompatible-element content, which is most consistent with their generation by high degrees of partial melting (30–50 per cent[3]). Current models for komatiite genesis include the melting of rock at great depth in plumes of hot, diapirically rising mantle[4] or the melting of relatively shallow mantle rocks at less extreme, but still high, temperatures caused by fluxing with water[5]. Here we report a suite of ultramafic lava flows from the Commondale greenstone belt, in the southern part of the Kaapvaal Craton, which represents a previously unrecognized type of komatiite with exceptionally high forsterite content of its igneous olivines, low TiO_2/Al_2O_3 ratio, high silica content, extreme depletion in rare-earth elements and low Re/Os ratio. We suggest a model for their formation in which a garnet-enriched residue left by earlier cratonic volcanism was melted by hydration from a subducting slab.

The well-preserved Commondale suite of lava flows, dated by whole-rock Sm–Nd at 3,334 ± 18 Myr age[6], contains spinifex textures and aphyric chill margins representing liquid compositions. The 600-m thick succession, comprising more than 80 flow units, has been intersected by diamond drilling, allowing complete units to be studied with unambiguous recognition of chill zones. Olivine and orthopyroxene are preferentially concentrated in the centres of the flows and both olivine and orthopyroxene spinifex occur near the top of the units, often in layered form. Olivine core compositions (higher than 96.5% forsterite content) have the highest magnesium content recorded for olivines in any naturally occurring terrestrial igneous rock. An abundance of primary liquidus orthopyroxene shows that these komatiites are different from all others previously described.

The Commondale liquids (Fig. 1) have high MgO (29–31%), high SiO_2 (49.5–50.5%) and extremely low iron contents (3.5–5% FeO). They are characterized by exceptionally low levels of incompatible elements (TiO_2 0.1%; Zr 2.6 p.p.m.; Y 5.2 p.p.m.; total rare-earth elements (REE) 2.9 p.p.m.) compared with other komatiites (TiO_2 0.3–1.61%; Zr 14–27 p.p.m.; Y 5–11 p.p.m.; total REE 9–19 p.p.m.). They also have the highest values for Al_2O_3/TiO_2 (65–95) recorded for any komatiite and exceptionally low Zr/Y (0.5 compared to 3.3 for Barberton-type komatiites). The latter is significant in that it indicates melting of a garnet-enriched mantle source. These lavas exhibit much greater light-REE depletion than the previously known most-extreme compositions, those of the Cretaceous komatiites of Gorgona Island (Fig. 2). Chondrite normalized values for Gd/Yb and La/Yb are 0.29 and 0.02 respectively, compared with 1–1.3 and 0.3–1.6 for other komatiites, including Barberton. The Commondale lavas are derived from a highly depleted and refractory mantle source of a type not previously recognized.

Commondale komatiites have extremely low Re (0.02–0.09 p.p.b.) and high Os (1–2 p.p.b.) contents that lead to low $^{187}Re/^{188}Os$ with a limited spread in Os isotopic composition (Fig. 3; Table 1). Although the samples show good linearity in the Re–Os isochron diagram, the limited range in the Re/Os produces a large uncertainty (440 Myr) about an age of 3,393 Myr, but this age agrees with the precise Sm–Nd isochron (3,334 ± 18 Myr age[6]). The low Re/Os of the samples tightly constrains the $^{187}Os/^{188}Os$ of their mantle source to 0.1047 ± 0.0017 ($\gamma_{Os} = 0.6 \pm 1.6$). This is equivalent to a source with a time-averaged chondritic Re/Os at 3,334 Myr ago. These Os isotopic compositions provide the best estimate until now of the Earth's oldest mantle composition obtained directly from a melt. The data confirm that the Earth's mantle had evolved from 4.5 to 3.3 Gyr ago with a chondritic time-averaged Re/Os and strongly supports a late chondritic veneer for highly siderophile elements[7–10]. A source of this composition gives no evidence of incorporation of radiogenic Os from the crust, a conclusion supported by the high initial Nd isotopic composition ($\epsilon_{Nd} = +2.0 \pm 0.7$)[6] and its extreme light-REE depletion. These

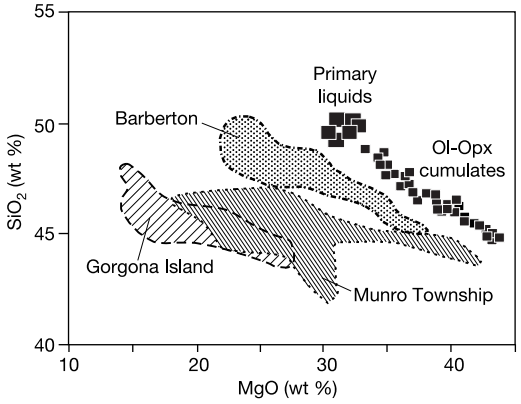

Figure 1 Variation of SiO_2 and MgO for Commondale liquid and olivine–orthopyroxene cumulates and for other komatiites. These are: Barberton komatiites[20]; komatiites from Munro Township (Abitibi belt)[21,22]; komatiites and picrites from Gorgona Island[2]. Ol, olivine; Opx, orthopyroxene.

